Computational Investigations of the Detailed Mechanism of Reverse Intersystem Crossing in Inverted Singlet-Triplet Gap Molecules

Danillo Valverde[1†‡], Cher Tian Ser[2,3†], Gaetano Ricci[1], Kjell Jorner[2,3,4§], Robert Pollice[2,3‖], Alán Aspuru-Guzik[2,3,5,6,7,8*], Yoann Olivier[1*]

[1]Laboratory for Computational Modeling of Functional Materials, Namur Institute of Structured Matter, Université de Namur, Rue de Bruxelles, 61, 5000 Namur, Belgium.
[2]Chemical Physics Theory Group, Department of Chemistry, University of Toronto, 80 St. George St, Toronto, Ontario M5S 3H6, Canada.
[3]Department of Computer Science, University of Toronto, 40 St. George St, Toronto, Ontario M5S 2E4, Canada.
[4]Department of Chemistry and Chemical Engineering, Chalmers University of Technology, Kemigård.
[5]Department of Chemical Engineering & Applied Chemistry, 200 College St., University of Toronto, Ontario M5S 3E5, Canada
[6]Department of Materials Science & Engineering, 184 College St., University of Toronto, Ontario M5S 3E4, Canada
[7]Vector Institute for Artificial Intelligence, 661 University Ave Suite 710, Toronto, Ontario M5G 1M1, Canada.
[8]Acceleration Consortium, 700 University Ave, Toronto, Ontario M5G 1Z5
[†]These authors contributed equally to this work.
[‡]Current address: Laboratory for Chemistry of Novel Materials, Université de Mons, Place du Parc, 20, 7000 Mons, Belgium.
[§]Current address: Institute of Chemical and Bioengineering, Department of Chemistry and Applied Biosciences, ETH Zurich, Vladimir-Prelog-Weg 1, CH-8093 Zürich, Switzerland
ETH Zurich.
[‖]Current address: Stratingh Institute for Chemistry, University of Groningen, Nijenborgh 4, Groningen, 9747 AG, The Netherlands.

Corresponding authors: yoann.olivier@unamur.be, alan@aspuru.com

Abstract

Inverted singlet-triplet gap (INVEST) materials have promising photophysical properties for optoelectronic applications due to an inversion of their lowest singlet (S_1) and triplet (T_1) excited states. This results in an exothermic reverse intersystem crossing (rISC) process that potentially enhances triplet harvesting, compared to thermally activated delayed fluorescence (TADF) emitters with endothermic rISCs. However, the processes and phenomena that facilitate conversion between

excited states for INVEST materials are underexplored. We investigate the complex potential energy surfaces (PESs) of the excited states of three heavily studied azaphenalene INVEST compounds, namely cyclazine, pentazine and heptazine using two state-of-the-art computational methodologies, namely RMS-CASPT2 and SCS-ADC(2) methods. Our findings suggest that ISC and rISC processes take place directly between the S_1 and T_1 electronic states in all three compounds through a minimum-energy crossing point (MECP) with an activation energy barrier between 0.11 to 0.58 eV above the S_1 state for ISC and between 0.06 to 0.36 eV above the T_1 state for rISC. We predict that higher-lying triplet states are not populated, since the crossing point structures to these states are not energetically accessible. Furthermore, the conical intersection (CI) between the ground and S_1 states are high in energy for all compounds (between 0.4 to 2.0 eV) which makes nonradiative decay back to the ground state a relatively slow process. We demonstrate that the spin-orbit coupling (SOC) driving the S_1-T_1 conversion is enhanced by vibronic coupling with higher-lying singlet and triplet states possessing vibrational modes of proper symmetry. We also rationalize that the experimentally-observed anti-Kasha emission of cyclazine is due to the energetically inaccessible CI between the bright S_2 and the dark S_1 states, hindering internal conversion. Finally, we show that SCS-ADC(2) is able to qualitatively reproduce excited state features, but consistently overpredict relative energies of excited state structural minima compared to RMS-CASPT2. The identification of these excited state features elaborates design rules for new INVEST emitters with improved emission quantum yields.

1. Introduction

OLEDs have received considerable attention for their large tunability of emission color and promising applications in thin and flexible displays. However, due to the spin statistics bottleneck for closed-shell fluorescent emitters, the internal quantum efficiency (IQE) of the first generation of singlet emissive excitons is limited to merely 25% during the hole-electron recombination process.[1] The remaining population (75% as triplet excitons) is lost through non-radiative decay. Various design strategies have been proposed to harvest a portion of this lost triplet population to overcome the spin-statistic limit.[2] Of these proposed strategies, thermally activated delayed fluorescence (TADF)[3] materials have attracted much attention recently as they can reach a theoretical IQE of 100% without precious heavy metals in their molecular composition. These materials rely on thermal excitations of triplet excitons into the singlet manifold of excited states via reverse intersystem crossing (rISC), which may only take place when there is significant spin-orbit coupling (SOC) between the singlet

and triplet manifold of states. Additionally, according to El-Sayed's rule,[4,5] the singlet and triplet states involved in rISC must bear the same nature to have non-zero SOCs. Facile rISC processes require a small gap between the lowest singlet (S_1) and triplet (T_1) excited states (ΔE_{ST}) (typically around 0.2 eV). However, typical closed-shell organic molecules possess T_1 states lower than S_1 states as described by Hund's first rule, which makes S_1 to T_1 intersystem crossing (ISC) more favorable than rISC.[6] ΔE_{ST} can be reduced through minimizing the exchange interaction energy, which is determined by the degree of overlap between the hole and electron densities associated with the lower lying singlet (S_1) and triplet (T_1) states. The first generation of TADF molecular emitters take advantage of this feature by introducing donor (D) and acceptor (A) units which involves lower excited states with a high intramolecular charge transfer (CT) character. Nonetheless, singlet CT states have weak to vanishing oscillator strength leading to small radiative emission cross sections and potentially low emission quantum yields. D-A TADF emitters also exhibit large conformational flexibilities, resulting in a broad emission spectrum impairing its color purity. Hence, multiple resonant (MR) TADF emitters[4] consisting of doped polyaromatic hydrocarbons were then proposed to improve color purity. Typically, the lower lying singlet and triplet states are short-range CT (SRCT) excited states characterized by electron transfer between neighboring atomic sites.

However, rISC in both design strategies remains an endothermic process. Past experimental studies on two nitrogen-containing triangulene analogues, i.e., cycl[3.3.3]azine[7] (cyclazine) and 1,4,7-triazacycl[3.3.3]azine,[8] showed unusual optoelectronic behavior with near-degenerate S_1 and T_1 states along with a short T_1 lifetime. A spectroscopic investigation on another nitrogen-containing triangulene analogue, namely 1,3,4,6,7,9,9b-heptaazaphenalene (heptazine),[9] provided no evidence of a T_1 state below the S_1 state, which is consistent with an inverted singlet-triplet energy gap and a violation of Hund's rule for closed-shell organic systems. Recently, in OLEDs made of heptazine derivatives, rISC was demonstrated to be an exothermic process as a consequence of an inverted ΔE_{ST} resulting in change of paradigm with respect to TADF compounds.[10–12] This new class of emitters of OLEDs is known as INVEST emitters.[13] Inverted singlet-triplet gaps have been theoretically predicted in conjugated hydrocarbons[14] and in their doped analogues,[15–24] further supported by several high-throughput virtual screening studies[13,25–27] that identified a series of new emitters for OLED applications based on these scaffolds that have both negative ΔE_{ST} and large oscillator strength. Microscopically, ΔE_{ST} originates from the sum of exchange (Fermi correlation) and Coulomb electron correlations, which contributes positively and negatively to ΔE_{ST} respectively.[23] Various propositions

have been made for the conditions or structural motifs required to achieve a negative ΔE_{ST} through the minimization of the exchange contributions, like doping to achieve high symmetry point groups[21] or double-bond delocalization.[19,28] However, inverted singlet-triplet gap predictions require correlated methodologies that include at least double excitations while some studies point to the need for the inclusion of triple-excitation with large basis sets,[29–32] to properly describe the stabilization of the S_1 state via dynamic spin polarization in these materials.[22] Indeed, single-excitation computational methods typically used in computational excited-state studies were unable to predict inverted singlet-triplet gaps.[9,23] We also note the recent success in using semiempirical methods to reproduce inverted singlet-triplet gaps.[29,33,34] The difficulty in modelling these systems computationally is exacerbated by the dearth of experimental literature on the photophysical properties of these systems.

The interconversion mechanism occurring between the triplet and singlet manifolds of excited states have previously been computationally investigated in heptazine and one of its derivatives.[16] In that study, rISC is considered to occur between T_1 and S_1 through a Herzberg-Teller (HT) mechanism where the SOC is enhanced by vibronic coupling to E″ vibrational modes. However, the contribution of higher-lying triplet excited states in INVEST materials remains unclear and has never been investigated systematically, although they have been identified to be key players in the rISC mechanism of TADF emitters. This would require specific investigations of the potential energy surfaces (PESs) of the singlet and triplet excited states as well as the possible crossings between them. With the aim to shed light on the photophysical mechanisms of INVEST emitters, we herein explore the PESs of cyclazine, pentazine and heptazine (**Figure 1**), three triangle-shaped azaphenalene compounds with computationally predicted inverted singlet-triplet gaps. We obtain geometries, energies, and the natures of excited-state structural minima, and both conical intersection (CI) and minimum-energy crossing point (MECP) ISC structures. We further geodesically interpolated[35] between the energy minima and their respective MECPs structures to obtain insights into the structural transformations that occur in the interconversion processes. Finally, we analyzed the influence of non-Condon effects for SOC required for S_1-T_1 conversions by considering vibronic coupling to higher-lying singlet and triplet states.

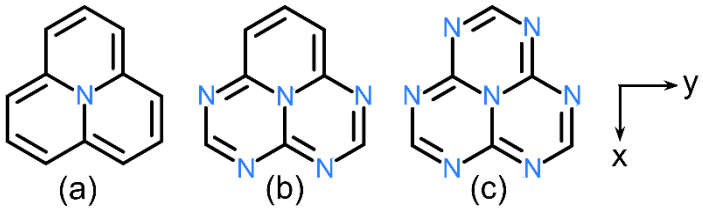

Figure 1: Schematic molecular structure of (a) cyclazine, (b) pentazine and (c) heptazine. The reference axes system adopted in this work is also illustrated.

2. Methodology

The use of wavefunction-based methods is of prime importance in INVEST materials in order to include to properly account for electron correlation effects that describe the inversion of the lower-lying singlet and triplet excited states.[15–24] Hence, singlet and triplet structures of all compounds were optimized with the Rotated Multi-State Complete-Active Space Second Order Theory (RMS-CASPT2)[36] method, based on a zeroth-order wavefunction computed with the state-averaged CASSCF (SA-CASSCF)[37] approach. The singlet and triplet regimes were state-averaged separately in their respective calculations. RMS-CASPT2 has been proven to be less dependent on the number of roots used in the calculation when compared with other CASPT2 variants.[38] We also test the accuracy of the second-order algebraic-diagrammatic construction combined with a spin-component scaling correction (SCS-ADC(2))[39–42] method. Single-reference methods, such as SCS-CC2 and SCS-ADC(2), are computationally cheaper than RMS-CASPT2 and can thus be applied to study larger systems, but were shown to predict larger negative ΔE_{ST}[21] for some compounds. However, the accuracy of these methods for the calculations of crossing points has never been tested before for this class of materials, and are hence worthy of investigation, especially in comparison to their lower computational cost. All calculations were performed with the def2-TZVP[43] atomic basis sets, and no symmetry restrictions were assumed. The resolution of identity (RI) approximation was employed for both levels of theory to speed up the computation of the two-electron integrals.[44] All RMS-CASPT2 calculations were carried out in OpenMolcas 23.02,[45] whereas SCS-ADC(2) calculations were run with the Turbomole 7.4 package.[46] An imaginary level shift[47] of 0.2 a.u. is introduced in RMS-CASPT2 to deal with possible intruder states, and, following a suggestion from the literature,[48] the ionization potential-electron affinity (IPEA) correction[49] is set to zero.

An active space comprising 12 electrons distributed over 12 orbitals is employed in the RMS-CASPT2 calculations (see **Figure S1**). The choice of the orbitals set and the size of the active space were based on the average orbital occupation numbers obtained from the SA-CASSCF calculation (threshold: between 0.02 and 1.98) so that only π and π* orbitals were included in this initial active space (see **Section 3.2** for further justification). Crossing points between states of either same or different multiplicities were computed as MECP structures between the potential energy surfaces of the two states of interest using both the RMS-CASPT2 and SCS-ADC(2) approaches. For RMS-CASPT2 optimizations, analytical nonadiabatic coupling (NAC) vectors were explicitly calculated, making the computed MECP structures true CIs. As the SCS-ADC(2) method does not provide NAC vectors, the Bearpark-Robb-Schlegel algorithm[50] was used to find MECP structures. These calculations were carried out with the SHARC (Surface Hopping including ARbitrary Couplings)[51] program which generates an interface between the selected quantum chemistry program (in our case Turbomole) and the external Orca optimizer.[52] SOC elements between singlet and triplet states were computed on the RMS-CASPT2 structures by combining density functional theory (DFT) in its time-dependent version within the Tamm-Dancoff approximation (TDA)[53] and PBE0[54] as DFT functional, def2-TZVP[43] basis set, and the one-electron Breit-Pauli operator[55] as implemented in Q-CHEM 5.3.[56] Normal mode analyses of the optimized ground and excited states geometries were carried out using MOMAP 2022a[57] using an undistorted displaced harmonic oscillator (DHO) model. In this case, both ground and excited states were reoptimized at the TDA-PBE0/def2-TZVP level.

3. Results and Discussions

3.1 Molecular orbital description and nature of the singlet and triplet excited states

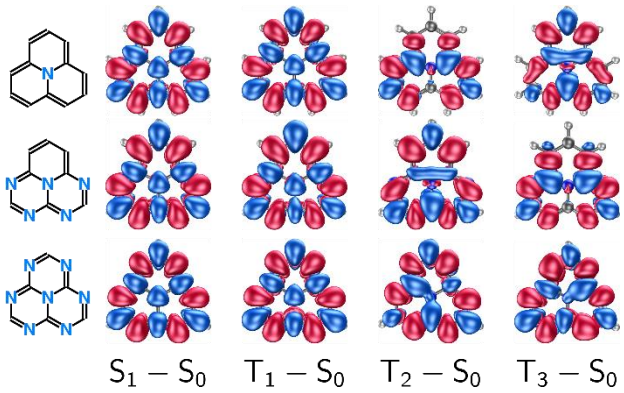

Figure 2*:* Difference density plots between the ground-state and the excited state of interest computed at the SA-CASSCF(12,12)/def2-TZVP level for cyclazine, pentazine, and cyclazine (the singlet and triplet manifolds are state-averaged separately). A similar pattern is also obtained at the SCS-ADC(2)/def2-TZVP considering the first singlet and the three triplet states (see **Figure S2**). A negative density difference value corresponds to red, while a positive density difference value corresponds to blue. An isovalue of 0.001 e/au^3 was used to plot the densities.

Despite the different nitrogen substitution patterns, the S_1 and T_1 excited states of all three molecules are predominantly described by a π-π^* electronic transition (**Table 1**) in which the SA-CASSCF(12,12) molecular orbitals (MOs) are disjoint and resemble the highest occupied MO (HOMO) and the lowest unoccupied MO (LUMO) predicted at the Hartree-Fock level, respectively (see **Figure S3**). The HOMO displays an exclusively non-bonding character localized on the edge of the triangulene core and the LUMO shows bonding character and a contribution on the central nitrogen atom (**Figure 2**). Interestingly, the difference density plots between S_1 and the ground state (S_0) as well as between T_1 and S_0 states revealed a SRCT pattern as previously observed in MR-TADF materials, supporting the observation that weak overlaps between hole and electron densities correlates with a small exchange energy (**Figure 2**).[58]

3.2 Vertical Excitation Energies

Table 1: Vertical excitation energies (ΔE_{FC}, eV), corresponding oscillator strength (*f*) and singlet-triplet energy gaps (ΔE_{ST}; eV) obtained at RMS-CASPT2(12,12)/def2-TZVP and SCS-ADC(2)/def2-

TZVP for cyclazine, pentazine and heptazine. Experimental absorption peaks are also reported for comparison. [a]Measured in hexane solution.[7] [b]Measured in chloroform for a series of pentazine derivatives.[59] [c]Measured in acetonitrile.[60]

Molecule	State	RMS-CASPT2(12,12)/def2-TZVP				SCS-ADC(2)/def2-TZVP				Exp.
		Nature	ΔE_{FC}	f	ΔE_{ST}	Nature	ΔE_{FC}	f	ΔE_{ST}	
Cyclazine	S_1	$^1(\pi\pi^*)$	0.89	$<1\times10^{-5}$	—	$^1(\pi\pi^*)$	1.08	0.000	—	1.0-1.5[a]
	S_2	$^1(\pi\pi^*)$	2.76	0.057	—	$^1(\pi\pi^*)$	3.17	0.281	—	2.6-3.0[a]
	T_1	$^1(\pi\pi^*)$	0.97	—	-0.08	$^1(\pi\pi^*)$	1.31	—	-0.23	
	T_2	$^1(\pi\pi^*)$	1.96	—	1.07	$^1(\pi\pi^*)$	2.35	—	1.27	
	T_3	$^1(\pi\pi^*)$	1.96	—	1.07	$^1(\pi\pi^*)$	2.35	—	1.27	
Pentazine	S_1	$^1(\pi\pi^*)$	2.00	0.002	—	$^1(\pi\pi^*)$	2.28	0.004	—	1.8-2.2[b]
	S_2	$^1(\pi\pi^*)$	3.36	0.084	—	$^1(\pi\pi^*)$	3.93	0.245	—	3.3-4.1[b]
	T_1	$^3(\pi\pi^*)$	2.08	—	-0.08	$^3(\pi\pi^*)$	2.51	—	-0.23	
	T_2	$^3(\pi\pi^*)$	2.75	—	0.75	$^3(\pi\pi^*)$	3.25	—	0.97	
	T_3	$^3(\pi\pi^*)$	2.92	—	0.92	$^3(\pi\pi^*)$	3.40	—	1.12	
Heptazine	S_1	$^1(\pi\pi^*)$	2.50	$<1\times10^{-5}$	—	$^1(\pi\pi^*)$	2.81	0.000	—	2.7[c]
	S_2	$^1(\pi\pi^*)$	3.99	0.122	—	$^1(n\pi^*)$	4.15	0.000	—	4.0[c]
	T_1	$^3(\pi\pi^*)$	2.70	—	-0.20	$^3(\pi\pi^*)$	3.19	—	-0.38	
	T_2	$^3(\pi\pi^*)$	3.35	—	0.85	$^3(\pi\pi^*)$	3.91	—	1.00	
	T_3	$^3(\pi\pi^*)$	3.35	—	0.85	$^3(\pi\pi^*)$	3.91	—	1.00	

Table 1 lists the vertical excitation energies of the lower two singlet and three triplet excited states of cyclazine, pentazine, and heptazine at the Franck-Condon (FC) region computed with the RMS-CASPT2 and SCS-ADC(2) methods. In general, RMS-CASPT2 provides vertical excitation energies lower than the SCS-ADC(2) method for all molecules. Both methods reproduce the expected hypsochromic shift going from cyclazine to pentazine and going from pentazine to heptazine. Both methods reveal that the S_1 transition has vanishing oscillator strength for both cyclazine and heptazine for symmetry reasons, and is only weakly allowed in pentazine which is in line with the low intensity absorption features measured experimentally.[59,61] Experimental lower absorption bands appear at energies around 1.0-1.5 eV and 2.6-3.0 eV for cyclazine[7] and heptazine[60] respectively, while our computations reasonably predict S_1 energies at 0.89 [1.08] eV and 2.50 [2.81] eV using RMS-CASPT2 [SCS-ADC(2)]. An intense absorption band is experimentally reported at ~2.7 eV and ~4.0 eV for cyclazine and heptazine, respectively, corresponding to the S_2 absorption at the RMS-CASPT2 calculations (see **Table 1**). In contrast, the strongly absorbing states at SCS-ADC(2) for heptazine and cyclazine correspond to S_5 and S_2, respectively, and are blue-shifted by 0.59 eV for heptazine and 0.47 eV for cyclazine with respect to the experiment. Both methods predict a negative ΔE_{ST} (**Table**

1) with SCS-ADC(2) giving the most negative gap in between the two methods, as previously demonstrated.[19,21] The ΔE_{ST} values obtained from RMS-CASPT2 (-0.08 eV for cyclazine, -0.08 eV for pentazine, and -0.20 eV for heptazine) are in good agreement with the best theoretical estimates proposed by Loos *et al.* (-0.13 eV for cyclazine, -0.12 eV for pentazine and -0.22 eV for heptazine),[32] obtained from vertical excitation energy calculations with CC3 and CCSDT methods. The RMS-CASPT2 ΔE_{ST} values are also in line with previous NEVPT2 ΔE_{ST} predictions.[15]

The S_2 excited state bears a $^1(n\pi^*)$ nature at the SCS-ADC(2)/def2-TZVP level for heptazine (weighting of 83%), with a vertical excitation energy of 4.07 eV. This is more than 1 eV above the S_1 state, which makes its contribution to spin interconversion via population of the S_2 state unlikely. Within the active space considered for our RMS-CASPT2 calculations, no nitrogen lone pair orbitals were included and hence only $\pi \rightarrow \pi^*$ transitions can be observed (see **Table 1**). To investigate if $n \rightarrow \pi^*$ transitions are relevant for RMS-CASPT2, we further increased the active space from (12,12) to (14,13) for heptazine and pentazine. In heptazine, we found $n \rightarrow \pi^*$ character for the S_2 state at RMS-CASPT2(12,12) level, in near resonance with the S_3 $^1(\pi\pi^*)$ state, 1.49 eV above S_1 (see **Table S1**) with no expected contribution to the spin interconversion mechanism as suggested by the calculations at the SCS-ADC(2) level of theory. In the case of pentazine, the $^1(n\pi^*)$ state is the S_3 state and is more than 2 eV above S_1 (see **Table S1**) and thus does not contribute directly to the spin interconversion mechanism. Since cyclazine does not have lone pair orbitals, the extension of the active space is not required. For cyclazine, the S_2-S_1 energy gap is predicted to be 1.87 eV with RMS-CASPT2(12,12) in good agreement with its absorption spectrum recorded in hexane solution (1.74 eV),[7] while it is slightly higherat the SCS-ADC(2) level (2.09 eV).

Turning to the triplets, T_2 and T_3 states are degenerate in both levels of theory for cyclazine and heptazine because of their D_{3h} symmetry, while this is not the case for pentazine. For cyclazine, the T_2 and T_3 states lie 0.99 [1.04] eV above the T_1 state according to RMS-CASPT2 [SCS-ADC(2)], while they are located 0.65 [0.72] eV higher than T_1 in the case of heptazine. This degeneracy is broken for pentazine, although the molecular orbitals that describe the T_2 and T_3 states are very similar to those observed for heptazine and cyclazine (see **Figure S4**). In this case, T_2 and T_3 are 0.67 [0.74] and 0.84 [0.89] eV above T_1. Overall, we observed a larger energy gap between S_1 and T_2 (ΔE_{S1T2}) at the SCS-ADC(2) level than at the RMS-CASPT2. Interestingly, the ΔE_{S1T2} gap is very large (in all

compounds larger than 0.7 eV) which makes the direct involvement of T_2 in a potential rISC mechanism unlikely.

3.3 ISC and rISC mechanisms

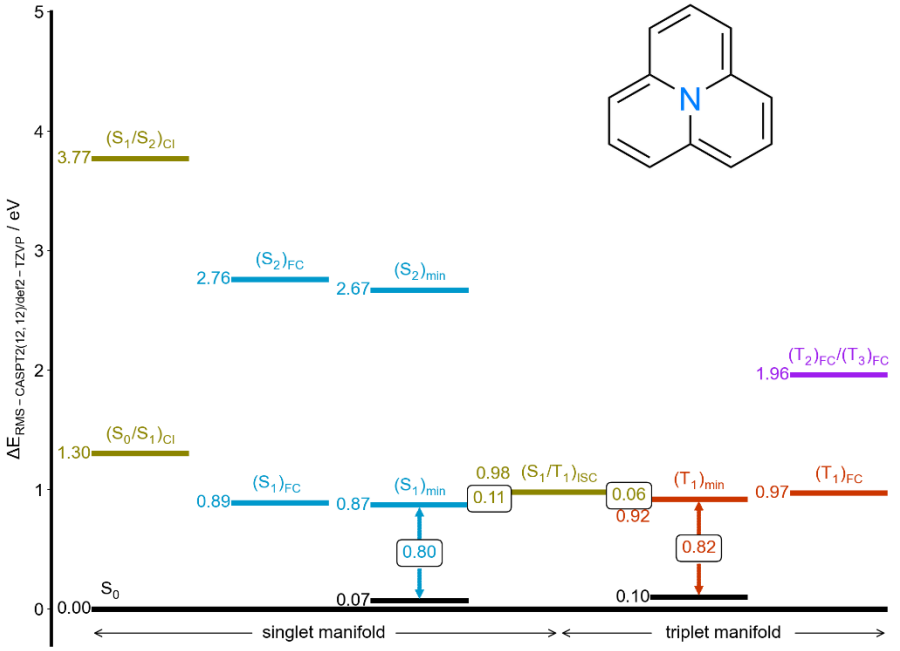

Figure 3: Jablonski diagram for cyclazine evaluated at the RMS-CASPT2(12,12)/def2-TZVP level of theory. SCS-ADC(2)/def2-TZVP values for cyclazine are plotted in **Figure S5**.

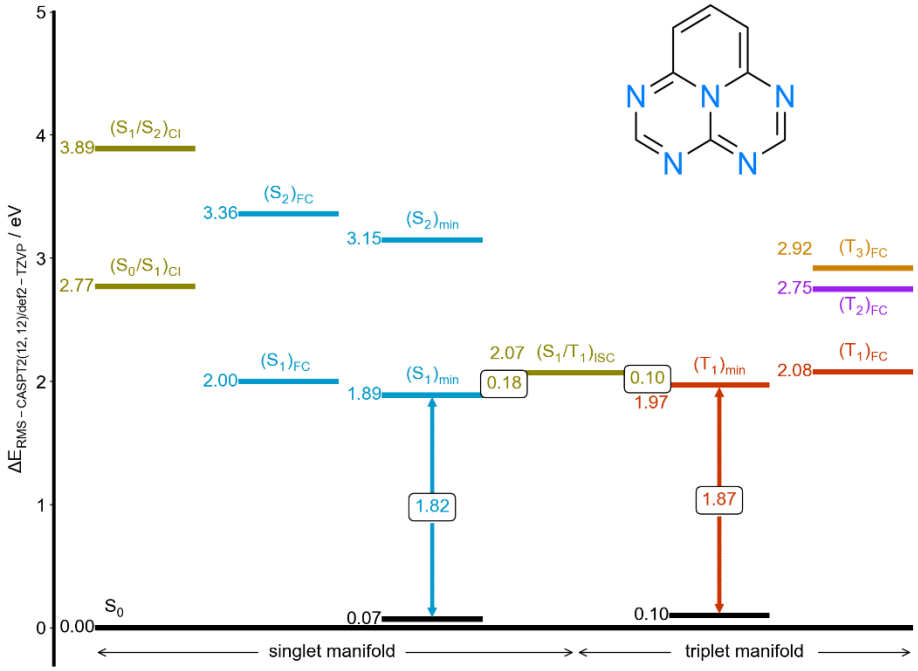

Figure 4: Jablonski diagram for pentazine evaluated at the RMS-CASPT2(12,12)/def2-TZVP level of theory. SCS-ADC(2)/def2-TZVP values for pentazine are plotted in **Figure S6**.

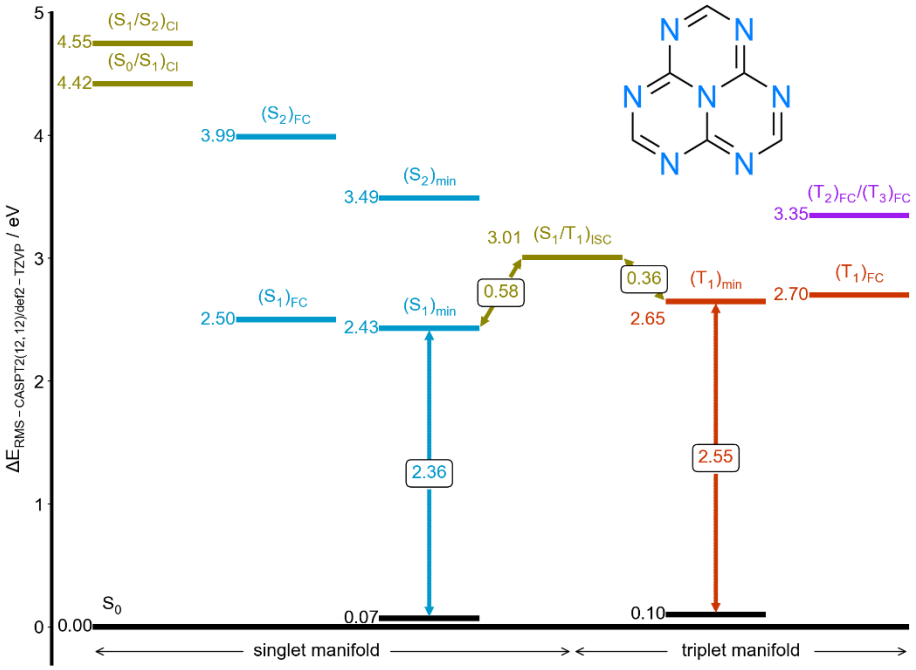

Figure 5: Jablonski diagram for heptazine evaluated at the RMS-CASPT2(12,12)/def2-TZVP level of theory. SCS-ADC(2)/def2-TZVP values for heptazine are plotted in **Figure S7**.

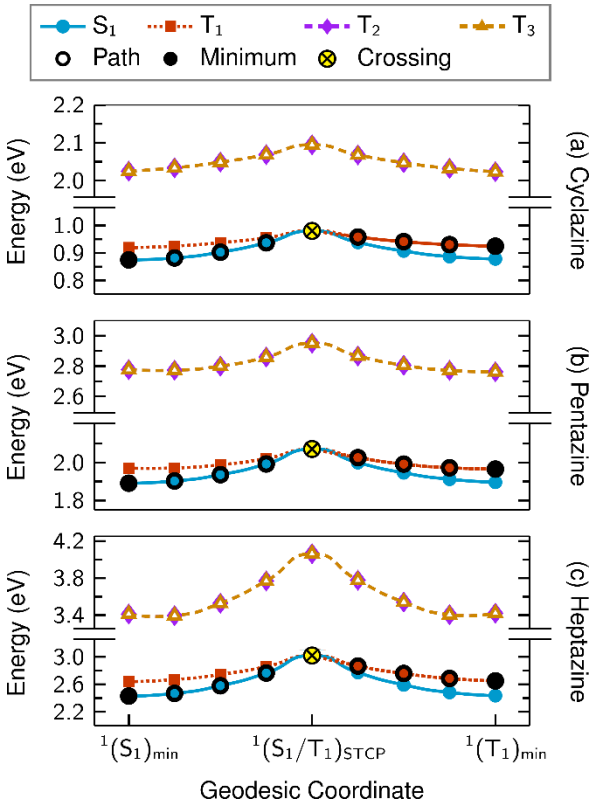

Figure 6*:* Geodesic interpolation pathways connecting optimized geometries and singlet-triplet crossing point for (a) cyclazine, (b) pentazine, and (c) heptazine computed at RMS-CASPT2/def2-TZVP level of theory. The relaxation paths are indicated with open black circles, minima with black circles and crossing points with X. SCS-ADC(2)/def2-TZVP interpolations are shown in **Figure S9**.

A complete understanding of the mechanistic aspects behind the rISC and ISC processes in these triangulene cores involves an estimation of the energy barrier as well as the magnitude of the SOC associated with the different conversion channels between the singlet and triplet excited states. This requires an exploration of the singlet and triplet excited state PESs beyond the FC region, and looking for the singlet-triplet crossing points (STCP) not only between S_1 and T_1 but potentially between S_1 and higher-lying triplet states T_n. To this end, we computed the relaxed geometries of the singlet and triplet excited state energy minima and the MECP (or CI for same-spin crossings where NACs are explicitly evaluated) structures between these PESs. Our results show that the minima of the S_1 and T_1 states closely resemble the ground state-optimized structure with retained planarity, and the most prominent changes are the changes in bond lengths of the aromatic rings. The relaxation energies from

the FC point to the S_1 and T_1 minima are rather small for both RMS-CASPT2 and SCS-ADC(2) (see **Table S2-3** and **Figure S8**). For S_1, the relaxation energies are 0.02, 0.11 and 0.07 eV for cyclazine (**Figure 3**), pentazine **(Figure 4)**, and heptazine **(Figure 5)** respectively for RMS-CASPT2, in line with what was previously reported for excited states exhibiting SRCT character.[18] For T_1, the relaxation energies are 0.05, 0.11 and 0.05 eV, for cyclazine, pentazine and heptazine respectively when computed with RMS-CASPT2. As a result, the adiabatic ΔE_{ST} computed at the RMS-CASPT2 level amounts to -0.05, -0.08 and -0.22 eV for cyclazine, pentazine, and heptazine, respectively.

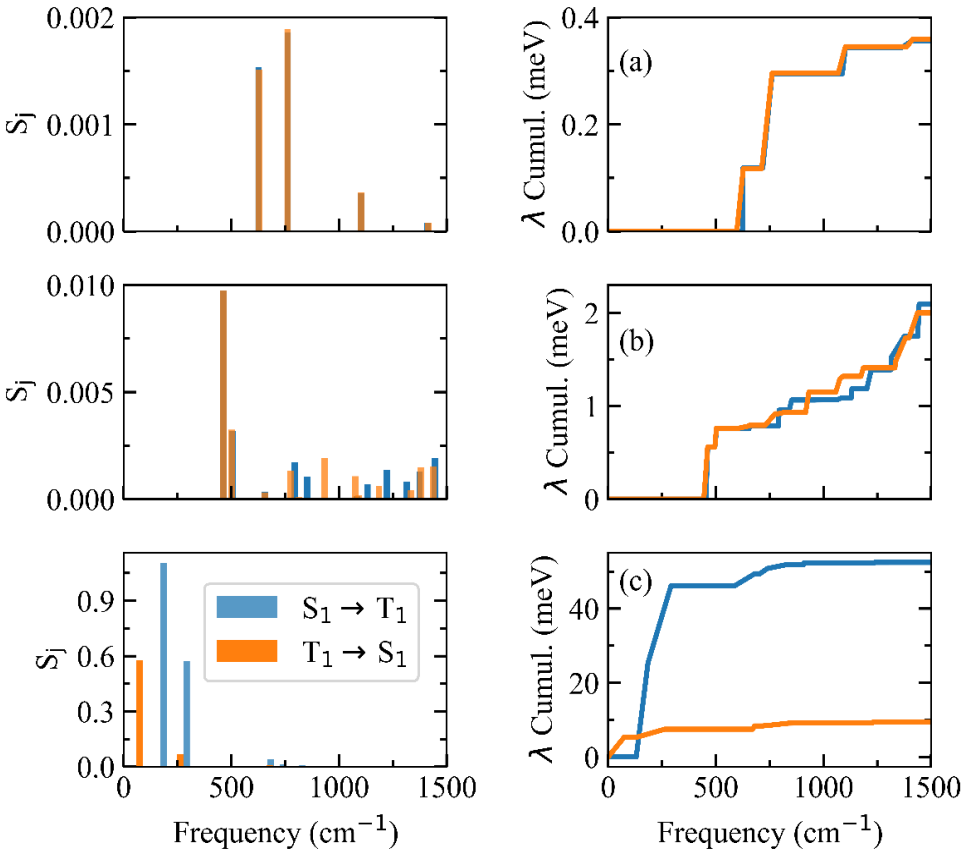

Figure 7*:* Huang-Rhys factor (left) and cumulative reorganization energy (right) computed at the TDA-PBE0/def2-TZVP level of theory for (a) cyclazine, (b) pentazine and (c) heptazine.

A STCP structure between the S_1 and T_1 states was found for all molecules. The STCP structures lie 0.11 and 0.06 eV, 0.18 and 0.11 eV, and 0.58 and 0.36 eV above the $(S_1)_{min}$ and $(T_1)_{min}$ for cyclazine, pentazine and heptazine respectively, at the RMS-CASPT2 level. As expected from the larger negative ΔE_{ST}, the crossing points obtained at SCS-ADC(2) are higher in energy compared to RMS-CASPT2,

by up to 0.1 eV (see **Table S3**). Since no crossing is found between the S_1 and the degenerate T_2 and T_3 PES along the geodesic scan (see **Figure 6**), ISC is expected to take place directly from S_1 to T_1. Interestingly, the ISC process is thermally activated with an energy barrier that grows with the number of nitrogen atoms per triangulene core (cyclazine → pentazine → heptazine). This is likely attributed to a small difference in the nature for S_1 and T_1 as witnessed by the slightly different difference density patterns of these two states (see **Figure S10**) which thus involve a crossing structure with a larger conformational change with respect to the minima. As witnessed by the computed energy barriers from the $(T_1)_{min}$ towards the S_1/T_1 STCP structure, rISC is also a thermally activated process, but it is still expected to occur on a faster timescale than ISC in view of the negative ΔE_{ST}.

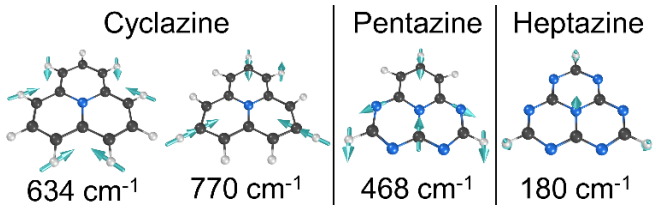

Figure 8*:* Normal modes associated with the highest Huang-Rhys factor for cyclazine, pentazine, and heptazine with their respective frequency.

We next computed the Huang-Rhys (HR) factors associated to the vibrational modes contributing to reorganization of the geometry of the three molecules upon ISC and rISC. The computed HR factors increase in magnitude when increasing the number of nitrogen atoms in the core of the selected triangulene compounds (see **Figure 7**). This further leads to a larger geometric distortion and thus larger reorganization energy associated with the ISC and rISC processes and thus a larger activation energy computed for heptazine. The opposite is true for cyclazine, where the lower geometric distortion leads to a lower activation energy. Furthermore, we identified the 770, 468, and 180 cm^{-1} normal modes for cyclazine, pentazine, and heptazine, respectively, as the dominant mode responsible for the geometry reorganization. Interestingly, the normal modes associated with the highest HR factor in the three compounds are similar for cyclazine and pentazine (see **Figure 8**), being predominantly described by the rocking motion of the hydrogen atoms together with the stretching of either the C-C bonds or the N-C bonds. In contrast, in heptazine, a vibrational mode with an out-of-plane motion of the central nitrogen atom factor which breaks the D_{3h} symmetry of the core contributes with the

highest HR factor. It is also worth mentioning that in cyclazine the normal mode with frequency of 634 cm^{-1}, described by the out-plane motion of some C-H bonds, also has a significant HR factor (see **Figure 8**).

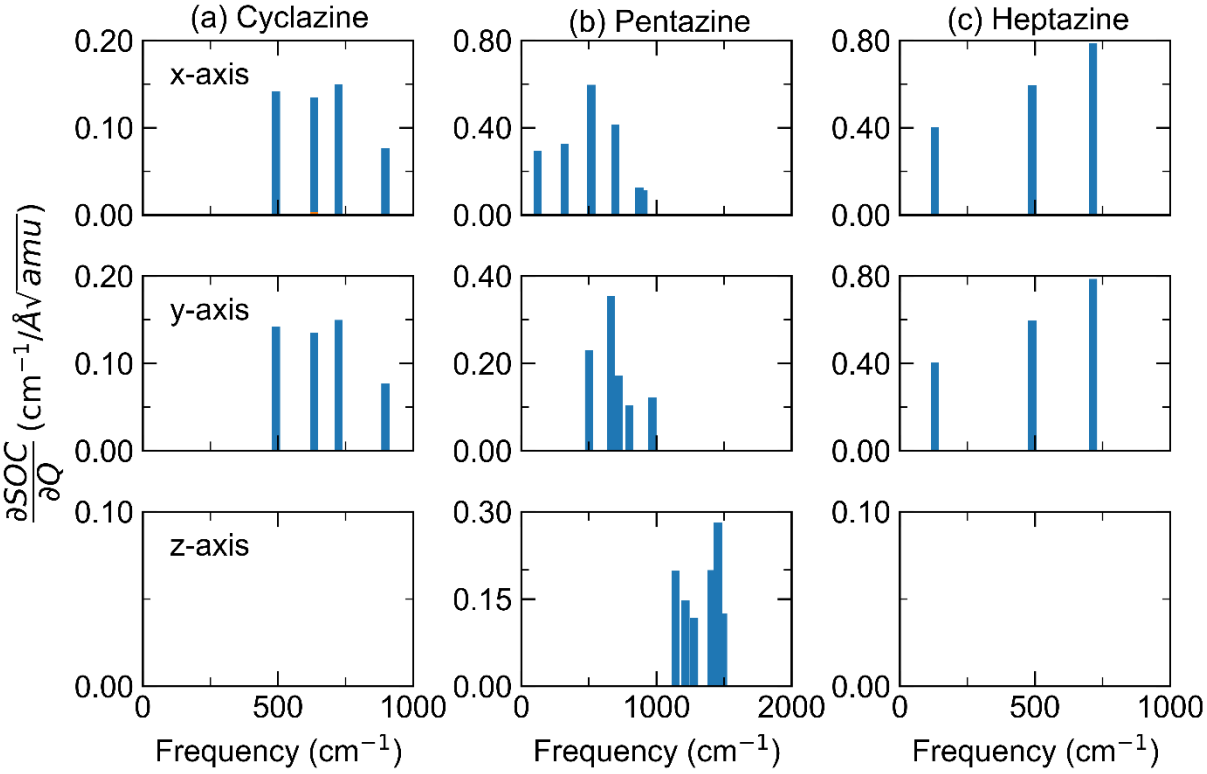

Figure 9*:* Electron-phonon coupling constants for each spin-orbit coupling (SOC) component computed as a function of the vibrational modes computed at the TDA-PBE0/def2-TZVP level of theory. We report only the imaginary part of the SOC since the real part vanishes. See **Figure 1** for reference axis.

We next evaluated the SOC for each of the three compounds. As the molecules possess the same electronic nature for both the S_1 and T_1 states, and that they possess high symmetry (D_{3h} for cyclazine and heptazine and C_{2v} for pentazine), the SOC computed at the S_1/T_1 crossing point for the three compounds vanishes (see **Tables S4, S5 and S6**). However, by including non-Condon effects within the linear vibronic coupling (LVC) regime, we could study the influence of vibrational modes on the magnitude of the SOC (see **Appendix S2**). In practice, we proceed by calculating the SOC along all normal modes distorting the equilibrium geometry of all molecules between -0.05 and 0.05 Å $\times \sqrt{\mu}$, where μ is the reduced mass associated with a given vibrational normal mode. We computed the

electron-phonon coupling constants of the α-th component of the SOC (SOC_α) associated with a given vibrational mode as the slope $\frac{\partial SOC_\alpha}{Q_i}$ of SOC_α (α = x, y, and z) as a function of the normal coordinate Q_i. We have also taken advantage of the D_{3h} symmetry that allows us to conclude, based on symmetry analysis, that only normal modes belonging to the A'_2 [E''] irreducible representation will affect SOC_z [SOC_x and SOC_y] for both cyclazine and heptazine (see **Tables S7-S12**). Pentazine has a lower symmetry and belongs to the C_{2v} point group so that SOC_x, SOC_y and SOC_z are affected by A_2, B_1 and B_2 modes (see **Tables S13-S15**). In **Figure 9**, we report the electron-phonon coupling constant associated with the i-th vibrational mode. For cyclazine and heptazine, only SOC_x and SOC_y are affected, or in other words, the SOC_z component is not impacted by any A'_2 vibrational normal mode. In the case of heptazine, the E'' normal modes at 490 and 733 cm^{-1} exhibit the largest electron-phonon coupling constants for the SOC_x and SOC_y components, even though they correspond to different atomic displacements for each component (see **Figure S11**, panels a and c). A similar trend is observed for cyclazine, with the E'' normal modes at 493, 633, and 725 cm^{-1} having the largest phonon coupling constants for both SOC_x and SOC_y. It is important to note that all normal modes that induce a large electron-phonon coupling constant for both heptazine and cyclazine involve out-of-plane distortions that break the D_{3h} symmetry. For pentazine, non-vanishing electron-phonon coupling constants are obtained for all components (see **Figure 9**). B_2 normal modes with frequencies above 1000 cm^{-1} contribute to SOC_z while A_2 and B_1 modes with frequencies below 1000 cm^{-1} affect SOC_x and SOC_y. We have identified the normal modes at 518, 662, and 1455 cm^{-1} with the highest electron coupling constants along the x-axis, y-axis, and z-axis, respectively. Our results suggest that A_2 vibrational modes are more strongly coupled to the SOC than B_1 and B_2 modes for pentazine. Interestingly, for pentazine, A_2 and B_1 normal modes that induce the largest SOC_x and SOC_y electron-phonon coupling constants are out-of-plane distortion similar to what is observed for both cyclazine and heptazine, whereas a rocking motion of a specific hydrogen atom associated with a B_2 mode along the y-axis leads to the largest electron-phonon coupling constant for SOC_z.

The thermalized SOC component can be calculated as follows:

$$\overline{SOC}_\alpha = \sqrt{(SOC_\alpha)^2 + \sigma_\alpha^2} \quad (1)$$

where σ_α^2 is the temperature-dependent vibrational correction to the α-th component of the SOC defined as:[62]

$$\sigma_{\alpha}^{2} = \sum_{i}^{3N-6} \frac{\hbar}{4\omega_i}\left(\frac{\partial SOC_{\alpha}}{\partial Q_i}\right)^{2} coth\left(\frac{\hbar\omega_i}{2k_B T}\right) \qquad \alpha \equiv x, y, z \qquad (2)$$

where the sum runs over all the 3N-6 normal modes, ω_i is the frequency associated with the i-th normal mode and T is the temperature.

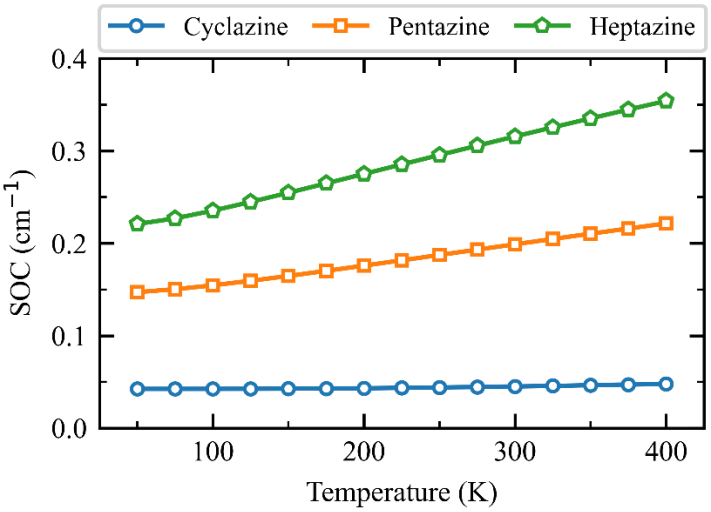

Figure 10*:* Total spin-orbit coupling (SOC) as a function of temperature including vibrational correction for (a) cyclazine, (b) pentazine, and (c) heptazine.

The vibrational corrections to the different components of the SOC at room temperature (σ_{α}^{2}) are larger in heptazine, for both the SOC_x and SOC_y components (**Table S4**). Unlike heptazine, the most notable contribution for pentazine comes from the SOC_x component (**Table S5**). Similar to heptazine, only the vibrational corrections to the SOC_x and SOC_y components contribute to the thermalized SOC components for cyclazine (**Table S6**), but this correction is around one order of magnitude smaller than for heptazine. By using expressions (1) and (2), we have computed the temperature-dependence of the total SOC value, as depicted in **Figure 10**. The temperature dependence of the SOC is more pronounced when increasing the nitrogen content from cyclazine to heptazine in line with the trends in the vibronic coupling associated with SOC. Our results suggest non-vanishing thermally activated SOC which amounts to 0.045, 0.199, and 0.316 cm^{-1} for cyclazine, pentazine, and heptazine respectively, at room temperature (300 K). It is worth noting that the SOC values obtained for pentazine and heptazine are similar in magnitude as the SOC obtained for TADF emitters.[63] These results suggest the presence of strong vibrational correction contributions in all three molecules that can substantially influence the ISC and rISC rate constants.

The different impacts of the vibrational modes on the SOC magnitude of the three compounds can be rationalized by developing the excited state wavefunction in an HT expansion. Through this, we can shed light on how vibrational modes enhance SOC by a borrowing effect originating from the vibronic coupling between the first excited state of each spin manifold with higher excited states of the same spin manifold (see SI for detailed information). In **Table S7**, we reported that the SOC enhancement in cyclazine comes from the vibronic coupling of T_1 with higher-lying triplet excited states, with the largest contribution coming from the coupling with T_6, via A_2' normal modes. SOC enhancement is also achieved in cyclazine via vibronic coupling of S_1 and the degenerate pairs $S_{5/6}$ via (E'') normal modes. As shown in **Table S9**, the larger SOC(T_1-$S_{5/6}$) compared to SOC(S_1-T_6), along with the smaller energy gap between T_1 and T_6 compared to S_1 and $S_{5/6}$, results in the E'' normal modes contributing more than the A_2' normal modes to the HT correction. This can be seen from the ratio $\frac{SOC}{(\varepsilon_{Sn/Tn}-\varepsilon_{S1/T1})}$, which is almost two orders of magnitude larger for SOC(T_1-$S_{5/6}$) compared to SOC(S_1-T_6), in line with the results shown in **Figure 9a**. In heptazine, only E'' normal modes induce vibronic coupling between S_1 and higher-lying singlets, and also for T_1 and higher-lying triplets (see **Table S10-S11**), rationalizing the vanishing electron-phonon contribution to SOC_z, which is associated with the A_2' normal modes (**Figure 9c**). Furthermore, the interplay between the energy gap between the vibronically active higher excited states of one spin manifold (S_n or T_n, respectively) and the first excited state of the same manifold (S_1 and T_1, respectively), and the SOC of these higher-lying excited states with the first excited state of the other spin manifold (T_1 and S_1, respectively) rationalizes the more prominent HT contribution in heptazine compared to cyclazine (**Figure 9a** and **9c**). For instance, by comparing **Table S9** and **Table S12,** it can be observed that in heptazine, the lowest vibronically-active singlet (triplet) states bear a larger SOC with T_1 (S_1) (> 5 cm^{-1}) and a smaller energy gap with S_1 (T_1) (< 1 eV) in comparison to cyclazine, where the sole vibronically active $S_{5/6}$ states are characterized by a smaller SOC with T_1 (3.39 cm^{-1}) and a larger energy gap with S_1 (> 2 eV) supporting the largest enhancement of SOC due to vibronic coupling in heptazine as compared to cyclazine. The same analysis can be carried out for pentazine, for which the less symmetrical core causes almost all the higher-lying singlet and triplet states to contribute to the SOC enhancement via vibronic coupling (**Table S13** and **Table S14**). As seen in **Table S15**, the lowest vibronically coupled states bearing a large SOC are T_4 and S_2 (6.87 cm^{-1} and 6.71 cm^{-1}) which are coupled by A_2 normal modes to T_1 and S_1, respectively. These states bring the largest contribution to the HT-enhanced SOC, as it can be

inferred from the ratio $\frac{SOC}{(\varepsilon_{Sn/Tn}-\varepsilon_{S1/T1})}$, rationalizing the largest electron-phonon coupling constants computed for SOC_x (**Figure 9b)**.

3.4 Internal conversion

The crossing structure between the ground and the first singlet states has been found for all molecules. This crossing structure is quite distorted compared to the planar S_0 and S_1 states, with the most striking feature being that the central nitrogen atom distorts out of the molecular plane (see **Figure 11**. This out-of-plane motion is energetically unfavorable due to the disruption of the π-system and the energetic barriers increase as the number of nitrogen atoms decreases. Using RMS-CASPT2 [SCS-ADC(2)], the barriers are 0.43 [0.39], 0.88 [0.81], and 1.99 [1.45] eV for cyclazine, pentazine and heptazine compared to their respective S_1 adiabatic minima. The high rigidity of these compounds supports the fact that the nonradiative decay mechanism towards the ground-state is a very slow process.

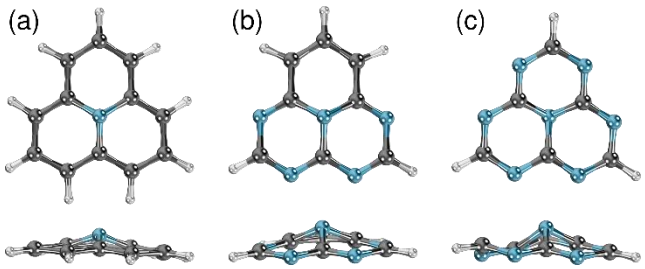

Figure 9: Front and side views of the $(S_1/S_0)_{CI}$ structure for (a) cyclazine, (b) pentazine and (c) heptazine computed at RMS-CASPT2(12,12)/def2-TZVP level. A similar structure with the central nitrogen outside the molecular plane is also found at the SCS-ADC(2)/def2-TZVP level (see **Figure S12**).

Cyclazine experimentally exhibits anti-Kasha emission when it is photoexcited to the S_2 state,[7] i.e., after the population of the S_2 state and the subsequent relaxation to the minimum of this state, the system remains excited long enough to release the excess energy through fluorescence. Our calculations predict an emission energy of 2.56 eV from the S_2 optimized minimum at the RMS-CASPT2(12,12)/def2-TZVP level in agreement with previous experimental data (~ 2.70 eV).[7] In order to better understand why cyclazine exhibits anti-Kasha behavior, we optimized the S_1/S_2 CI structure. According to RMS-CASPT2, the S_1/S_2 crossing point lies high in energy at 1.10 eV above the S_2 state

energy minimum, in line with the considerably distorted structure (see **Figure S13**). These findings allow us to conclude that the emission from the S_2 is more likely than the S_2-S_1 IC, especially in view of the oscillator strength of 0.059 that suggests via spontaneous Einstein emission rate a radiative decay time constant in the ~50 ns timescale. We can infer that a similar photophysical behaviour should occur for pentazine and heptazine since a large activation energy from the S_2 energy minimum towards the S_1/S_2 CI is also computed (0.74 eV for pentazine and 1.06 eV for heptazine at RMS-CASPT2 level) and a large oscillator strength that amounts to 0.087 and 0.145 for pentazine and heptazine, respectively suggesting radiative decay time constants for both compounds in the >~10 nstimescale. As proposed by Veys and Escudero[64] and Padula et *al.*,[65] a well-accepted rule of thumb for dominant anti-Kasha $S_2 \rightarrow S_0$ emission from certain classes of molecules is a large S_2-S_1 energy gap which results in a very slow internal conversion $S_2 \rightarrow S_1$. This condition is achieved here for cyclazine, pentazine and heptazine with an adiabatic energy gap between S_1-S_2 as large as 1.80, 1.26 and 1.06 eV at the RMS-CASPT2 level. Unfortunately, there are no experimental results yet for pentazine and heptazine that could validate our theoretical predictions.

4. Conclusions

In this study, we explored in detail the singlet and triplet excited state PESs of three heavily-studied INVEST compounds through a static computational approach, which consists of the geometry optimizations of relevant critical point structures, *i.e.*, energy minima, conical intersections and minimum-energy crossing points between states of same and different multiplicities, and (r)ISCs between singlets and triplets as well as computing the SOC between the relevant excited states involved in the (r)ISC process. We evidenced several features of these materials as well as some methodological aspects which should be accounted for people with interest in the computational design of new INVEST molecules:

1. *From the understanding of the ISC and rISC mechanisms per se:*
    a. Only the S_1 and T_1 states are directly populated in the ISC and rISC processes of these three compounds since there were no found crossing points between S_1 and higher-lying triplet states as predicted by both RMS-CASPT2 and SCS-ADC(2).
    b. While higher singlet and triplet states are not explicitly populated during ISC and rISC, they contribute by enhancing the otherwise vanishing SOC between the S_1 and T_1

through vibronic coupling. A careful symmetry analysis allowed us to rationalize both the magnitude of the electron-phonon coupling constants associated with each of the three SOC components and the vibrational modes contributing to them.

c. Even though we considered unsubstituted INVEST compounds, we believe that vibronic coupling in the singlet and the triplet manifolds of excited states is a general rule of thumb in increasing the magnitude of SOC between relevant excited states in INVEST compounds. INVEST compounds available in the literature for OLEDs applications usually bear substituents which are usually quite flexible and can bring additional vibronic coupling to SOC[18].

d. However, a rISC mechanism involving a direct conversion from T_1 to S_1 is likely not general for INVEST. In contrast to the three cores investigated here, functionalized cores can lead to the presence of lower-lying singlet and triplet associated with the substituents, potentially leading to a denser manifold of singlet and triplet excited states with multiple crossings between states of the same or different multiplicities.

2. *From the understanding of the IC mechanisms occurring in the singlet manifold of excited states:*

   a. The anti-Kasha behavior observed experimentally in cyclazine is due to the high energy barrier from S_2 adiabatic minimum towards the S_1-S_2 CI. Similarly, we predicted that anti-Kasha behavior for pentazine and heptazine is likely to occur.

   b. The nonradiative decay to the ground state is unlikely in view of the large energy barrier from the S_1 to the S_1-S_0 conical intersection for all molecules considered in this study. A high energy barrier for INVEST compounds requires an apparent rigidity of the molecular core, as supported by the small relaxation energy and thus a small change in the molecular geometry to go from S_1 to S_0.

3. *From a methodological point of view:* The investigation of the PES of these three compounds using the single-reference SCS-ADC(2) method results in the same qualitative interpretation of the mechanistic aspects of the ISC and rISC processes, although the magnitudes of the energy barriers associated with ISC and rISC are all higher compared to RMS-CASPT2, and the magnitudes of IC barriers are lower.

We hope that the conclusions derived from this study will aid efforts in the computational modelling of bright INVEST molecules and help the forefront development of these materials.

Data availability

All input and output files for optimized geometries and energies evaluated at the RMS-CASPT2/def2-TZVP and SCS-ADC(2)/def2-TZVP levels of theory, and optimized geometries and frequencies at the TDA-PBE0/def2-TZVP level of theory are made accessible via an ioChem-BD[66] database hosted at https://iochem-bd.matter.toronto.edu/.

Acknowledgements

This research used resources of the "Plateforme Technologique de Calcul Intensif (PTCI)" (http://www.ptci.unamur.be) located at the University of Namur, Belgium, which is supported by the FNRS-FRFC, the Walloon Region, and the University of Namur (Conventions No. 2.5020.11, GEQ U.G006.15, 1610468, RW/GEQ2016 et U.G011.22). The PTCI is member of the "Consortium des Équipements de Calcul Intensif (CÉCI)" (http://www.ceci-hpc.be). Computations were also made on the supercomputer Narval from École de technologie supérieure, managed by Calcul Québec and the Digital Research Alliance of Canada. The operation of this supercomputer is funded by the Canada Foundation for Innovation (CFI), Ministère de l'Économie, des Sciences et de l'Innovation du Québec (MESI) and le Fonds de recherche du Québec – Nature et technologies (FRQ-NT). D.V and Y.O. acknowledges funding by the Fonds de la Recherche Scientifique-FNRS under Grant n° F.4534.21 (MIS-IMAGINE). G. R. acknowledges a grant from the ''Fonds pour la formation a la Recherche dans l'Industrie et dans l'Agriculture'' (FRIA) of the FRS-FNRS. R.P. acknowledges funding through a Postdoc.Mobility fellowship by the Swiss National Science Foundation (SNSF, Project No. 191127). K.J. acknowledges funding through an International Postdoc grant from the Swedish Research Council (no. 2020-00314). A.A.-G. acknowledges support from the CIFAR, the Acceleration Consortium, the Canada 150 Research Chairs Program as well as Anders G. Fröseth. We thank Stefano Battaglia for fruitful discussions on use of an early version of RMS-CASPT2 in OpenMolcas.

References

(1) Hong, G.; Gan, X.; Leonhardt, C.; Zhang, Z.; Seibert, J.; Busch, J. M.; Bräse, S. A Brief History of OLEDs—Emitter Development and Industry Milestones. *Adv Mater* **2021**, *33* (9), 2005630. https://doi.org/10.1002/adma.202005630.

(2) Ha, J. M.; Hur, S. H.; Pathak, A.; Jeong, J.-E.; Woo, H. Y. Recent Advances in Organic Luminescent Materials with Narrowband Emission. *NPG Asia Mater* **2021**, *13* (1), 53. https://doi.org/10.1038/s41427-021-00318-8.

(3) Uoyama, H.; Goushi, K.; Shizu, K.; Nomura, H.; Adachi, C. Highly Efficient Organic Light-Emitting Diodes from Delayed Fluorescence. *Nature* **2012**, *492* (7428), 234–238. https://doi.org/10.1038/nature11687.
(4) El-Sayed, M. A. Spin—Orbit Coupling and the Radiationless Processes in Nitrogen Heterocyclics. *J. Chem. Phys.* **1963**, *38* (12), 2834–2838.
(5) Lower, S. K.; El-Sayed, M. A. The Triplet State and Molecular Electronic Processes in Organic Molecules. *Chem. Rev.* **1966**, *66* (2), 199–241. https://doi.org/10.1021/cr60240a004.
(6) Hund, F. Zur Deutung verwickelter Spektren, insbesondere der Elemente Scandium bis Nickel. *Z. Für Phys.* **1925**, *33* (1), 345–371. https://doi.org/10.1007/BF01328319.
(7) Leupin, W.; Wirz, J. Low-Lying Electronically Excited States of Cycl[3.3.3]Azine, a Bridged 12.Pi.-Perimeter. *J Am Chem Soc* **1980**, *102* (19), 6068–6075. https://doi.org/10.1021/ja00539a016.
(8) Leupin, W.; Magde, D.; Persy, G.; Wirz, J. 1,4,7-Triazacycl[3.3.3]Azine: Basicity, Photoelectron Spectrum, Photophysical Properties. *J Am Chem Soc* **1986**, *108* (1), 17–22. https://doi.org/10.1021/ja00261a004.
(9) Ehrmaier, J.; Rabe, E. J.; Pristash, S. R.; Corp, K. L.; Schlenker, C. W.; Sobolewski, A. L.; Domcke, W. Singlet–Triplet Inversion in Heptazine and in Polymeric Carbon Nitrides. *J Phys Chem A* **2019**, *123* (38), 8099–8108. https://doi.org/10.1021/acs.jpca.9b06215.
(10) Aizawa, N.; Pu, Y.-J.; Harabuchi, Y.; Nihonyanagi, A.; Ibuka, R.; Inuzuka, H.; Dhara, B.; Koyama, Y.; Nakayama, K.; Maeda, S.; Araoka, F.; Miyajima, D. Delayed Fluorescence from Inverted Singlet and Triplet Excited States. *Nature* **2022**, *609* (7927), 502–506. https://doi.org/10.1038/s41586-022-05132-y.
(11) Li, J.; Zhang, Q.; Nomura, H.; Miyazaki, H.; Adachi, C. Thermally Activated Delayed Fluorescence from 3Nπ* to 1Nπ∗ Up-Conversion and Its Application to Organic Light-Emitting Diodes. *Appl Phys Lett* **2014**, *105* (1). https://doi.org/10.1063/1.4887346.
(12) Li, J.; Nakagawa, T.; Macdonald, J.; Zhang, Q.; Nomura, H.; Miyazaki, H.; Adachi, C. Highly Efficient Organic Light-Emitting Diode Based on a Hidden Thermally Activated Delayed Fluorescence Channel in a Heptazine Derivative. *Adv Mater* **2013**, *25* (24), 3319–3323. https://doi.org/10.1002/ADMA.201300575.
(13) Pollice, R.; Friederich, P.; Lavigne, C.; dos Passos Gomes, G.; Aspuru-Guzik, A. Organic Molecules with Inverted Gaps between First Excited Singlet and Triplet States and Appreciable Fluorescence Rates. *Matter* **2021**, *4* (5), 1654–1682.
(14) Koseki, S.; Nakajima, T.; Toyota, A. Violation of Hund's Multiplicity Rule in the Electronically Excited States of Conjugated Hydrocarbons. *Can J Chem* **1985**, *63* (7), 1572–1579. https://doi.org/10.1139/v85-267.
(15) Ricci, G.; San-Fabián, E.; Olivier, Y.; Sancho-García, J. C. Singlet-Triplet Excited-State Inversion in Heptazine and Related Molecules: Assessment of TD-DFT and Ab Initio Methods. *ChemPhysChem* **2021**, *22* (6), 553–560. https://doi.org/10.1002/cphc.202000926.
(16) Pios, S.; Huang, X.; Sobolewski, A. L.; Domcke, W. Triangular Boron Carbon Nitrides: An Unexplored Family of Chromophores with Unique Properties for Photocatalysis and Optoelectronics. *Phys Chem Chem Phys* **2021**, *23* (23), 12968–12975. https://doi.org/10.1039/D1CP02026A.
(17) Sobolewski, A. L.; Domcke, W. Are Heptazine-Based Organic Light-Emitting Diode Chromophores Thermally Activated Delayed Fluorescence or Inverted Singlet–Triplet Systems? *J Phys Chem Lett* **2021**, *12* (29), 6852–6860. https://doi.org/10.1021/acs.jpclett.1c01926.

(18) Dinkelbach, F.; Bracker, M.; Kleinschmidt, M.; Marian, C. M. Large Inverted Singlet–Triplet Energy Gaps Are Not Always Favorable for Triplet Harvesting: Vibronic Coupling Drives the (Reverse) Intersystem Crossing in Heptazine Derivatives. *J Phys Chem A* **2021**, *125* (46), 10044–10051. https://doi.org/10.1021/acs.jpca.1c09150.
(19) Terence Blaskovits, J.; Garner, M. H.; Corminboeuf, C. Symmetry-Induced Singlet-Triplet Inversions in Non-Alternant Hydrocarbons. *Angew Chem Int Ed* **2023**, *62* (15). https://doi.org/10.1002/anie.202218156.
(20) Sanz-Rodrigo, J.; Ricci, G.; Olivier, Y.; Sancho-García, J. C. Negative Singlet–Triplet Excitation Energy Gap in Triangle-Shaped Molecular Emitters for Efficient Triplet Harvesting. *J Phys Chem A* **2021**, *125* (2), 513–522. https://doi.org/10.1021/acs.jpca.0c08029.
(21) Ricci, G.; Sancho-García, J.-C.; Olivier, Y. Establishing Design Strategies for Emissive Materials with an Inverted Singlet–Triplet Energy Gap (INVEST): A Computational Perspective on How Symmetry Rules the Interplay between Triplet Harvesting and Light Emission. *J Mater Chem C* **2022**, *10* (35), 12680–12698. https://doi.org/10.1039/D2TC02508F.
(22) Kollmar, H.; Staemmler, V. Violation of Hund's Rule by Spin Polarization in Molecules. *Theor Chim Acta* **1978**, *48* (3), 223–239. https://doi.org/10.1007/BF00549021.
(23) Silva, P. Inverted Singlet-Triplet Gaps and Their Relevance to Thermally Activated Delayed Fluorescence. *J Phys Chem Lett* **2019**, *10* (18), 5674–5679. https://doi.org/10.1021/acs.jpclett.9b02333.
(24) Liu, S.; Langenaeker, W. Hund's Multiplicity Rule: A Unified Interpretation. *Theor Chem Acc* **2003**, *110* (5), 338–344. https://doi.org/10.1007/s00214-003-0487-6.
(25) Omar, Ö. H.; Xie, X.; Troisi, A.; Padula, D. Identification of Unknown Inverted Singlet-Triplet Cores by High-Throughput Virtual Screening. *J Am Chem Soc* **2023**, *145* (36), 19790–19799. https://doi.org/10.1021/jacs.3c05452.
(26) Pollice, R.; Ding, B.; Aspuru-Guzik, A. Rational Design of Organic Molecules with Inverted Gaps between the First Excited Singlet and Triplet. *Matter* **2023**.
(27) Nigam, A.; Pollice, R.; Friederich, P.; Aspuru-Guzik, A. Artificial Design of Organic Emitters via a Genetic Algorithm Enhanced by a Deep Neural Network. *Chem. Sci.* **2024**. https://doi.org/10.1039/D3SC05306G.
(28) Garner, M. H.; Blaskovits, J. T.; Corminboeuf, C. Double-Bond Delocalization in Non-Alternant Hydrocarbons Induces Inverted Singlet–Triplet Gaps. *Chem Sci* **2023**, *14* (38), 10458–10466. https://doi.org/10.1039/D3SC03409G.
(29) Bedogni, M.; Giavazzi, D.; Maiolo, F.; Painelli, A. Shining Light on Inverted Singlet–Triplet Emitters. *J Chem Theory Comput* **2023**. https://doi.org/10.1021/acs.jctc.3c01112.
(30) Dreuw, A.; Hoffmann, M. The Inverted Singlet–Triplet Gap: A Vanishing Myth? *Front Chem* **2023**, 11. https://doi.org/10.3389/fchem.2023.1239604.
(31) Monino, E.; Loos, P.-F. Connections and Performances of Green's Function Methods for Charged and Neutral Excitations, 2023. https://doi.org/10.1063/5.0159853.
(32) Loos, P.-F.; Lipparini, F.; Jacquemin, D. H. Cyclazine, and Related Compounds: Chemically-Accurate Estimates of the Inverted Singlet–Triplet Gap. *J Phys Chem Lett* **2023**, *14* (49), 11069–11075. https://doi.org/10.1021/acs.jpclett.3c03042.
(33) Jorner, K.; Pollice, R.; Lavigne, C.; Aspuru-Guzik, A. Ultrafast Computational Screening of Molecules with Inverted Singlet-Triplet Energy Gaps Using the Pariser-Parr-Pople Semi-Empirical Quantum Chemistry Method. ChemRxiv September 25, 2023. https://doi.org/10.26434/chemrxiv-2023-wq1tb.

(34) Drwal, D.; Matousek, M.; Golub, P.; Tucholska, A.; Hapka, M.; Brabec, J.; Veis, L.; Pernal, K. Role of Spin Polarization and Dynamic Correlation in Singlet–Triplet Gap Inversion of Heptazine Derivatives. *J. Chem. Theory Comput.* **2023**, *19* (21), 7606–7616. https://doi.org/10.1021/acs.jctc.3c00781.
(35) Zhu, X.; Thompson, K. C.; Martínez, T. J. Geodesic Interpolation for Reaction Pathways. *J Chem Phys* **2019**, *150* (16). https://doi.org/10.1063/1.5090303/198363.
(36) Battaglia, S.; Lindh, R. On the Role of Symmetry in XDW-CASPT2. *J Chem Phys* **2021**, 154 3. https://doi.org/10.1063/5.0030944.
(37) Roos, B. O. The Complete Active Space Self-Consistent Field Method and Its Applications in Electronic Structure Calculations. *AB Initio Methods Quantum Chem - II* **2007**, *69*, 399–445. https://doi.org/10.1002/9780470142943.CH7.
(38) Nishimoto, Y.; Battaglia, S.; Lindh, R. Analytic First-Order Derivatives of (X)MS, XDW, and RMS Variants of the CASPT2 and RASPT2 Methods. *J Chem Theory Comput* **2022**, *18* (7), 4269–4281. https://doi.org/10.1021/acs.jctc.2c00301.
(39) Schirmer, J. Beyond the Random-Phase Approximation: A New Approximation Scheme for the Polarization Propagator. *Phys Rev A* **1982**, *26* (5), 2395–2416. https://doi.org/10.1103/PhysRevA.26.2395.
(40) Trofimov, A. B.; Schirmer, J. An Efficient Polarization Propagator Approach to Valence Electron Excitation Spectra. *J Phys B Mol Opt Phys* **1995**, *28* (12), 2299–2324. https://doi.org/10.1088/0953-4075/28/12/003.
(41) Dreuw, A.; Wormit, M. The Algebraic Diagrammatic Construction Scheme for the Polarization Propagator for the Calculation of Excited States. *Wiley Interdiscip Rev Comput Mol Sci* **2015**, *5* (1), 82–95. https://doi.org/10.1002/wcms.1206.
(42) Winter, N. O. C.; Hättig, C. Scaled Opposite-Spin CC2 for Ground and Excited States with Fourth Order Scaling Computational Costs. *J. Chem. Phys.* **2011**, *134* (18), 184101. https://doi.org/10.1063/1.3584177.
(43) Schäfer, A.; Huber, C.; Ahlrichs, R. Fully Optimized Contracted Gaussian Basis Sets of Triple Zeta Valence Quality for Atoms Li to Kr. *J Chem Phys* **1994**, *100* (8), 5829–5835. https://doi.org/10.1063/1.467146.
(44) Aquilante, F.; Lindh, R.; Bondo Pedersen, T. Unbiased Auxiliary Basis Sets for Accurate Two-Electron Integral Approximations. *J Chem Phys* **2007**, *127* (11), 114107. https://doi.org/10.1063/1.2777146.
(45) Fdez. Galván, I.; Vacher, M.; Alavi, A.; Angeli, C.; Aquilante, F.; Autschbach, J.; Bao, J. J.; Bokarev, S. I.; Bogdanov, N. A.; Carlson, R. K.; Chibotaru, L. F.; Creutzberg, J.; Dattani, N.; Delcey, M. G.; Dong, S. S.; Dreuw, A.; Freitag, L.; Frutos, L. M.; Gagliardi, L.; Gendron, F.; Giussani, A.; González, L.; Grell, G.; Guo, M.; Hoyer, C. E.; Johansson, M.; Keller, S.; Knecht, S.; Kovačević, G.; Källman, E.; Li Manni, G.; Lundberg, M.; Ma, Y.; Mai, S.; Malhado, J. P.; Malmqvist, P. Å.; Marquetand, P.; Mewes, S. A.; Norell, J.; Olivucci, M.; Oppel, M.; Phung, Q. M.; Pierloot, K.; Plasser, F.; Reiher, M.; Sand, A. M.; Schapiro, I.; Sharma, P.; Stein, C. J.; Sørensen, L. K.; Truhlar, D. G.; Ugandi, M.; Ungur, L.; Valentini, A.; Vancoillie, S.; Veryazov, V.; Weser, O.; Wesołowski, T. A.; Widmark, P.-O. O.; Wouters, S.; Zech, A.; Zobel, J. P.; Lindh, R. OpenMolcas: From Source Code to Insight. *J Chem Theory Comput* **2019**, *15* (11), 5925–5964. https://doi.org/10.1021/acs.jctc.9b00532.
(46) Furche, F.; Ahlrichs, R.; Hättig, C.; Klopper, W.; Sierka, M.; Weigend, F. T. Wiley Interdiscip. *Rev Comput Mol Sci* **2014**, *4* (2), 91–100. https://doi.org/10.1002/WCMS.1162.

(47) Forsberg, N.; Malmqvist, P.-Å. Å. Multiconfiguration Perturbation Theory with Imaginary Level Shift. *Chem Phys Lett* **1997**, *274* (1–3), 196–204. https://doi.org/10.1016/S0009-2614(97)00669-6.
(48) Zobel, J. P.; Nogueira, J. J.; González, L. The IPEA Dilemma in CASPT2. *Chem Sci* **2017**, *8* (2), 1482–1499. https://doi.org/10.1039/C6SC03759C.
(49) Ghigo, G.; Roos, B. O.; Malmqvist, P.-Å. A Modified Definition of the Zeroth-Order Hamiltonian in Multiconfigurational Perturbation Theory (CASPT2. *Chem Phys Lett* **2004**, *396* (1–3), 142–149. https://doi.org/10.1016/j.cplett.2004.08.032.
(50) Bearpark, M. J.; Robb, M. A.; Bernhard Schlegel, H. A Direct Method for the Location of the Lowest Energy Point on a Potential Surface Crossing. *Chem Phys Lett* **1994**, *223* (3), 269–274. https://doi.org/10.1016/0009-2614(94)00433-1.
(51) Richter, M.; Marquetand, P.; González-Vázquez, J.; Sola, I.; González, L. SHARC: Ab Initio Molecular Dynamics with Surface Hopping in the Adiabatic Representation Including Arbitrary Couplings. *J Chem Theory Comput* **2011**, *7* (5), 1253–1258. https://doi.org/10.1021/ct1007394.
(52) Neese, F. The ORCA Program System. *WIREs Comput Mol Sci* **2012**, *2* (1), 73–78. https://doi.org/10.1002/wcms.81.
(53) Taylor, J. C. Tamm-Dancoff Method. *Phys Rev* **1954**, *95* (5), 1313–1317. https://doi.org/10.1103/PhysRev.95.1313.
(54) Adamo, C.; Barone, V. Toward Reliable Density Functional Methods without Adjustable Parameters: The PBE0 Model. *J Chem Phys* **1999**, *110* (13), 6158–6170. https://doi.org/10.1063/1.478522.
(55) Mann, J. B.; Johnson, W. R. Breit Interaction in Multielectron Atoms. *Phys Rev A* **1971**, *4* (1), 41–51. https://doi.org/10.1103/PhysRevA.4.41.
(56) Shao, Y.; Gan, Z.; Epifanovsky, E.; Gilbert, A. T. B.; Wormit, M.; Kussmann, J.; Lange, A. W.; Behn, A.; Deng, J.; Feng, X.; Ghosh, D.; Goldey, M.; Horn, P. R.; Jacobson, L. D.; Kaliman, I.; Khaliullin, R. Z.; Kuš, T.; Landau, A.; Liu, J.; Proynov, E. I.; Rhee, Y. M.; Richard, R. M.; Rohrdanz, M. A.; Steele, R. P.; Sundstrom, E. J.; Woodcock, H. L.; Zimmerman, P. M.; Zuev, D.; Albrecht, B.; Alguire, E.; Austin, B.; Beran, G. J. O.; Bernard, Y. A.; Berquist, E.; Brandhorst, K.; Bravaya, K. B.; Brown, S. T.; Casanova, D.; Chang, C. M.; Chen, Y.; Chien, S. H.; Closser, K. D.; Crittenden, D. L.; Diedenhofen, M.; Distasio, R. A.; Do, H.; Dutoi, A. D.; Edgar, R. G.; Fatehi, S.; Fusti-Molnar, L.; Ghysels, A.; Golubeva-Zadorozhnaya, A.; Gomes, J.; Hanson-Heine, M. W. D.; Harbach, P. H. P.; Hauser, A. W.; Hohenstein, E. G.; Holden, Z. C.; Jagau, T. C.; Ji, H.; Kaduk, B.; Khistyaev, K.; Kim, J.; Kim, J.; King, R. A.; Klunzinger, P.; Kosenkov, D.; Kowalczyk, T.; Krauter, C. M.; Lao, K. U.; Laurent, A. D.; Lawler, K. V.; Levchenko, S. V.; Lin, C. Y.; Liu, F.; Livshits, E.; Lochan, R. C.; Luenser, A.; Manohar, P.; Manzer, S. F.; Mao, S. P.; Mardirossian, N.; Marenich, A. V.; Maurer, S. A.; Mayhall, N. J.; Neuscamman, E.; Oana, C. M.; Olivares-Amaya, R.; Oneill, D. P.; Parkhill, J. A.; Perrine, T. M.; Peverati, R.; Prociuk, A.; Rehn, D. R.; Rosta, E.; Russ, N. J.; Sharada, S. M.; Sharma, S.; Small, D. W.; Sodt, A.; Stein, T.; Stück, D.; Su, Y. C.; Thom, A. J. W.; Tsuchimochi, T.; Vanovschi, V.; Vogt, L.; Vydrov, O.; Wang, T.; Watson, M. A.; Wenzel, J.; White, A.; Williams, C. F.; Yang, J.; Yeganeh, S.; Yost, S. R.; You, Z. Q.; Zhang, I. Y.; Zhang, X.; Zhao, Y.; Brooks, B. R.; Chan, G. K. L.; Chipman, D. M.; Cramer, C. J.; Goddard, W. A.; Gordon, M. S.; Hehre, W. J.; Klamt, A.; Schaefer, H. F.; Schmidt, M. W.; Sherrill, C. D.; Truhlar, D. G.; Warshel, A.; Xu, X.; Aspuru-Guzik, A.; Baer, R.; Bell, A. T.; Besley, N. A.; Chai, J. D.; Dreuw, A.; Dunietz, B. D.; Furlani, T. R.; Gwaltney, S. R.; Hsu, C. P.; Jung, Y.; Kong, J.; Lambrecht, D. S.; Liang, W.; Ochsenfeld, C.; Rassolov, V. A.; Slipchenko, L. V.;

Subotnik, J. E.; Voorhis, T.; Herbert, J. M.; Krylov, A. I.; Gill, P. M. W.; Head-Gordon, M. Advances in Molecular Quantum Chemistry Contained in the Q-Chem 4 Program Package, 2014, *113*, 184–215. https://doi.org/10.1080/00268976.2014.952696.

(57) Niu, Y.; Li, W.; Peng, Q.; Geng, H.; Yi, Y.; Wang, L.; Nan, G.; Wang, D.; Shuai, Z. MOlecular MAterials Property Prediction Package (MOMAP) 1.0: A Software Package for Predicting the Luminescent Properties and Mobility of Organic Functional Materials. *Mol Phys* **2018**, *116* (7–8), 1078–1090. https://doi.org/10.1080/00268976.2017.1402966.

(58) Pershin, A.; Hall, D.; Lemaur, V.; Sancho-Garcia, J.-C.; Muccioli, L.; Zysman-Colman, E.; Beljonne, D.; Olivier, Y. Highly Emissive Excitons with Reduced Exchange Energy in Thermally Activated Delayed Fluorescent Molecules. *Nat. Commun.* **2019**, *10* (1), 597. https://doi.org/10.1038/s41467-019-08495-5.

(59) Watanabe, H.; Tanaka, K.; Chujo, Y. Independently Tuned Frontier Orbital Energy Levels of 1,3,4,6,9b-Pentaazaphenalene Derivatives by the Conjugation Effect. *J. Org. Chem.* **2019**, *84* (5), 2768–2778. https://doi.org/10.1021/acs.joc.8b03161.

(60) Halpern, A. M.; Rossman, M. A.; Hosmane, R. S.; Leonard, N. J. Photophysics of the S1 .Tautm. SO Transition in Tri-s-Triazine. *J Phys Chem* **1984**, *88* (19), 4324–4326. https://doi.org/10.1021/j150663a026.

(61) Watanabe, H.; Hirose, M.; Tanaka, K.; Tanaka, K.; Chujo, Y. Color Tuning of Alternating Conjugated Polymers Composed of Pentaazaphenalene by Modulating Their Unique Electronic Structures Involving Isolated-LUMOs. *Polym. Chem.* **2016**, *7* (22), 3674–3680. https://doi.org/10.1039/C6PY00685J.

(62) Sánchez-Carrera, R. S.; Paramonov, P.; Day, G. M.; Coropceanu, V.; Brédas, J.-L. Interaction of Charge Carriers with Lattice Vibrations in Oligoacene Crystals from Naphthalene to Pentacene. *J Am Chem Soc* **2010**, *132* (41), 14437–14446. https://doi.org/10.1021/ja1040732.

(63) Olivier, Y.; Yurash, B.; Muccioli, L.; D'Avino, G.; Mikhnenko, O.; Sancho-García, J. C.; Adachi, C.; Nguyen, T. Q.; Beljonne, D. Nature of the Singlet and Triplet Excitations Mediating Thermally Activated Delayed Fluorescence. *Phys. Rev. Mater.* **2017**, *1* (7), 075602. https://doi.org/10.1103/PhysRevMaterials.1.075602.

(64) Veys, K.; Escudero, D. Anti-Kasha Fluorescence in Molecular Entities: Central Role of Electron–Vibrational Coupling. *Acc Chem Res* **2022**, *55* (18), 2698–2707. https://doi.org/10.1021/acs.accounts.2c00453.

(65) Omar, Ö. H.; Nematiaram, T.; Troisi, A.; Padula, D. Organic Materials Repurposing, a Data Set for Theoretical Predictions of New Applications for Existing Compounds. *Sci Data* **2022**, *9* (1), 54. https://doi.org/10.1038/s41597-022-01142-7.

(66) Álvarez-Moreno, M.; de Graaf, C.; López, N.; Maseras, F.; Poblet, J. M.; Bo, C. Managing the Computational Chemistry Big Data Problem: The ioChem-BD Platform. *J. Chem. Inf. Model.* **2015**, *55* (1), 95–103. https://doi.org/10.1021/ci500593j.